In: 2023 IEEE International Radar Conference (RADAR), 6-10 november, Sydney, Australia
DOI: 10.1109/RADAR54928.2023.10371178

Multistatic dual-channel detection of drones: effects of PNT errors

Benjamin Griffin* Alessio Balleri**, Aled Catherall*
*Plextek, Great Chesterford, Saffron Walden, UK
**Centre for Electronic Warfare, Information and Cyber, Cranfield University,
Defence Academy of the United Kingdom, Shrivenham, SN6 8LA

***Abstract*—A radar network solution to detect drones is presented that consists of low-cost low-size dual-channel moving receivers, which can be deployed on UASs and operate within the coverage of an existing cooperative or non-cooperative monostatic staring radar. The receivers exploit the use of a dual-channel design and therefore use a reference and a surveillance channel to operate coherently without the requirement of a shared synchronisation reference signal between the network nodes, which is one of the key limitations of other traditional multistatic radar network solutions. Drone detection and parameter estimation is achieved by fusing the information collected at the network receivers and rely on accurate Position, Navigation and Timing (PNT) information. In this paper, we investigate the effects of PNT errors on estimation performance for such a radar network.**

***Index Terms*—PNT, Data Fusion, Drone Detection, Multistatic, Radar**

I. Introduction

Staring radars use a transmitting static wide-beam antenna and a directive digital array to form multiple simultaneous beams on receive. Because the transmitting beam is wide and fixed, t he r adar c an e mploy l ong i ntegration t imes t o detect slow and low-RCS targets, such as drones, which present a challenge to traditional surveillance radars with a rotating mechanical antenna or electronic scanning [1].

Despite the long integration benefits, s taring r adars suffer from severe multipath and clutter effects against low-RCS low-altitude targets. A radar network solution consisting of low-cost low-size dual-channel receivers can be deployed on UASs and operate within the coverage of an existing cooperative or non-cooperative monostatic staring radar. The network receivers exploit the use of a dual-channel design and therefore use a reference and a surveillance channel to operate coherently without the requirement of a shared synchronisation reference signal between the network nodes, which is one of the key limitations of traditional multistatic radar network solutions. This reduces the requirement for receivers to maintain both time and frequency synchronisation with the transmitter, which not only simplifies the system design considerations but also enables exploitation of opportunistic and non-cooperative transmission sources [2] [3] [4].

Because the receiver nodes operate independently, the only interaction required between the nodes in the network is represented by the comms signals used to share radar data and Position, Navigation and Timing (PNT) information to enable data fusion from disparate receivers and ultimately provide target detections [5]. The dual-channel feature of this concept allows the development of independent low Size Weight, Power and Cost (SWaP-C) receivers and significantly facilitates deployment on moving platforms, such as low SWaP UAVs. Ultimately, the design provides a low-cost self-synchronising coherent network solution, simplifying the problem of ensuring receivers are operating synchronously with the transmitter(s). In this paper, the effects of Position-Timing and Navigation (PNT) errors on two types of data fusion schemes is investigated. A centralised *IQ-Fusion* is compared with a distributed *Detection-Fusion* approach for varying levels of PNT errors.

II. Network and Signal Model

Consider a multistatic radar network consisting of a cooperative monostatic staring radar, a target, and N moving dual-channel receivers. Each receiver is capable of forming two antenna beams to collect the direct signal from the staring transmitter and the target echoes. These beams can be generated using two separate physical antennas or with phased array multibeam techniques.

The target state vector (position and velocity) on a Cartesian plane is indicated with

$$\boldsymbol{\theta} = \begin{pmatrix} x & y & z & \dot{x} & \dot{y} & \dot{z} \end{pmatrix}^{\mathsf{T}} \tag{1}$$

while the state vectors of the i-th receiver are indicated with

$$\boldsymbol{p}_i = \begin{pmatrix} x_i & y_i & z_i & \dot{x}_i & \dot{y}_i & \dot{z}_i \end{pmatrix}^{\mathsf{T}} \tag{2}$$

where $i = 1, .., N$. The state vector of the cooperative monostatic transmitting radar is $\boldsymbol{p}_0$ and is assumed to be stationary ($\dot{x}_0 = \dot{y}_0 = \dot{z}_0 = 0$).

Define two 3x6 matrices

$$\boldsymbol{U} = \begin{pmatrix} 1 & 0 & 0 & 0 & 0 & 0 \\ 0 & 1 & 0 & 0 & 0 & 0 \\ 0 & 0 & 1 & 0 & 0 & 0 \end{pmatrix} \tag{3a}$$

$$\boldsymbol{V} = \begin{pmatrix} 0 & 0 & 0 & 1 & 0 & 0 \\ 0 & 0 & 0 & 0 & 1 & 0 \\ 0 & 0 & 0 & 0 & 0 & 1 \end{pmatrix} \tag{3b}$$

The bistatic time-delay and Doppler shift of the target with respect to the i-th receiver are

$$\tau_i(\boldsymbol{\theta}) = \frac{1}{c}\left(\sqrt{\langle \boldsymbol{U}(\boldsymbol{p}_0-\boldsymbol{\theta}), \boldsymbol{U}(\boldsymbol{p}_0-\boldsymbol{\theta})\rangle} + \sqrt{\langle \boldsymbol{U}(\boldsymbol{p}_i-\boldsymbol{\theta}), \boldsymbol{U}(\boldsymbol{p}_i-\boldsymbol{\theta})\rangle}\right) \tag{4a}$$

$$f_i(\boldsymbol{\theta}) = \frac{1}{\lambda}\left(\frac{\langle \boldsymbol{V}\boldsymbol{\theta}, \boldsymbol{U}(\boldsymbol{p}_0-\boldsymbol{\theta})\rangle}{\sqrt{\langle \boldsymbol{U}(\boldsymbol{p}_0-\boldsymbol{\theta}), \boldsymbol{U}(\boldsymbol{p}_0-\boldsymbol{\theta})\rangle}} + \frac{\langle \boldsymbol{V}\boldsymbol{\theta}, \boldsymbol{U}(\boldsymbol{p}_i-\boldsymbol{\theta})\rangle}{\sqrt{\langle \boldsymbol{U}(\boldsymbol{p}_i-\boldsymbol{\theta}), \boldsymbol{U}(\boldsymbol{p}_i-\boldsymbol{\theta})\rangle}} - \frac{\langle \boldsymbol{V}\boldsymbol{p}_i, \boldsymbol{U}(\boldsymbol{p}_i-\boldsymbol{\theta})\rangle}{\sqrt{\langle \boldsymbol{U}(\boldsymbol{p}_i-\boldsymbol{\theta}), \boldsymbol{U}(\boldsymbol{p}_i-\boldsymbol{\theta})\rangle}}\right) \tag{4b}$$

where c is the speed of light in a vacuum and $\langle\cdot,\cdot\rangle$ denotes the inner product between two vectors. The first two terms of equation (4b) are due to the relative motion of the target with respect to the transmitter and i-th receiver, while the third term is due to the motion of the receiver.

III. Target Dynamics

The target's dynamics are modelled using a nearly constant velocity model with discrete white noise acceleration [6]. The state vector of the target contains the target's position and velocity (1).

The target motion is modelled with a linear state transition equation as

$$\boldsymbol{\theta}_n = \boldsymbol{F}\boldsymbol{\theta}_{n-1} + \boldsymbol{w} \tag{5}$$

where $\boldsymbol{\theta}_n$ is the target's state at time-step n and $\boldsymbol{w}$ is the process noise with covariance $\boldsymbol{Q}$. The state transition matrix $\boldsymbol{F}$ is defined as

$$\boldsymbol{F} = \begin{pmatrix} 1 & 0 & 0 & \Delta t & 0 & 0 \\ 0 & 1 & 0 & 0 & \Delta t & 0 \\ 0 & 0 & 1 & 0 & 0 & \Delta t \\ 0 & 0 & 0 & 1 & 0 & 0 \\ 0 & 0 & 0 & 0 & 1 & 0 \\ 0 & 0 & 0 & 0 & 0 & 1 \end{pmatrix} \tag{6}$$

where Δt is the simulation time-step, equivalent to the coherent processing interval. A continuous white noise acceleration motion model is assumed [6] and therefore the process noise covariance matrix is

$$\boldsymbol{Q} = \begin{pmatrix} \frac{1}{3}\Delta t^3 & 0 & 0 & \frac{1}{2}\Delta t^2 & 0 & 0 \\ 0 & \frac{1}{3}\Delta t^3 & 0 & 0 & \frac{1}{2}\Delta t^2 & 0 \\ 0 & 0 & \frac{1}{3}\Delta t^3 & 0 & 0 & \frac{1}{2}\Delta t^2 \\ \frac{1}{2}\Delta t^2 & 0 & 0 & \Delta t & 0 & 0 \\ 0 & \frac{1}{2}\Delta t^2 & 0 & 0 & \Delta t & 0 \\ 0 & 0 & \frac{1}{2}\Delta t^2 & 0 & 0 & \Delta t \end{pmatrix} q \tag{7}$$

where q is a filter tuning parameter.

IV. PNT Errors

The successful fusion of the measurements made by the receivers into an estimate of the target's state requires knowledge of the state of the transmitter and the state of each of the receivers. While in practice, the position of a static transmitter can be known to a high level of accuracy, obtaining the same level of accuracy for moving receivers is a much more complex challenge. While the development of Global Satellite Navigation Systems (GNSS) has made this problem somewhat easier to solve, these systems are not flawless, and errors are inherent, subsequently impacting the data fusion process and the final estimate of the target's state.

TABLE I: PNT Error Levels

PNT Error	Position Error [m]	Velocity Error [m/s]
Level 0	0	0
Level 1	3.6	1
Level 2	10	5

Table I lists three levels of increasing PNT errors; the level 1 position error is based on the typical performance of GPS [7]. PNT errors are introduced by adding a zero mean, multivariate Gaussian random vector to the receivers' state vectors to obtain

$$\hat{\boldsymbol{p}}_i = \boldsymbol{p}_i + \boldsymbol{v}_i, \qquad \boldsymbol{v}_i \sim \mathcal{N}(\boldsymbol{0}, \Sigma) \tag{8}$$

where $\hat{\boldsymbol{p}}_i$ is the i-th receiver's state vector with PNT errors. The covariance matrix of the PNT error is

$$\Sigma = \begin{pmatrix} \sigma_p^2 & 0 & 0 & 0 & 0 & 0 \\ 0 & \sigma_p^2 & 0 & 0 & 0 & 0 \\ 0 & 0 & \sigma_p^2 & 0 & 0 & 0 \\ 0 & 0 & 0 & \sigma_v^2 & 0 & 0 \\ 0 & 0 & 0 & 0 & \sigma_v^2 & 0 \\ 0 & 0 & 0 & 0 & 0 & \sigma_v^2 \end{pmatrix} \tag{9}$$

where σ_p and σ_v are the position and velocity standard deviations of the PNT error term and correspond to the values in Table I.

It is worth observing that the target state CRLB derived assuming perfect knowledge of the state of the transmitter and all the receivers can only be used to model the first level of PNT errors (PNT Error Level 0). However, PNT errors can be incorporated into the Maximum Likelihood Estimator (MLE) and used to find a PNT-CRLB [8]. The approximated bound can then be used to generate the appropriate measurements for the various levels of PNT error for the data fusion scheme employed.

V. IQ-Fusion Scheme

The IQ-Fusion scheme combines the received signals from all the receiver nodes centrally to estimate the targets state in an single step using the MLE. The IQ-Fusion scheme has the advantage that all the received target's energy is concentrated into a single point before the detector and therefore the target

SNR can be significantly greater than the Detection-Fusion scheme, enabling detection of the target at greater ranges.

The measurement model at time step n is given by:

$$\boldsymbol{z}_n = \boldsymbol{\theta}_n + \boldsymbol{e}_n, \qquad \boldsymbol{e}_n \sim \mathcal{N}(\mathbf{0}, \text{CRLB}(\boldsymbol{\theta}_n)) \tag{10}$$

where $\boldsymbol{\theta}_n$ is the target's true state at time step n and $\boldsymbol{e}_n$ is the measurement error at time step n. The measurement error is modelled as a multivariate Gaussian distribution with zero mean and covariance matrix equal to the CRLB of the target's state evaluated at time step n. Note that the CRLB depends not only on the target's state but also on the state of the transmitters and receivers.

A. Kalman Filter

The Kalman filter is used to combine estimates of the target's state vector over time to determine the targets trajectory. Between successive time steps (coherent processing intervals) the estimate of the target's state and the state error covariance is predicted according to:

$$\hat{\boldsymbol{\theta}}_{n|n-1} = \boldsymbol{F}\hat{\boldsymbol{\theta}}_{n-1|n-1} \tag{11a}$$

$$\boldsymbol{P}_{n|n-1} = \boldsymbol{F}\boldsymbol{P}_{n-1|n-1}\boldsymbol{F}^T + \boldsymbol{Q}_n \tag{11b}$$

where $\hat{\boldsymbol{\theta}}_{n|n-1}$ is the estimate of the target's state at time step n incorporating all measurements up to and including time step $n-1$ and $\boldsymbol{P}_{n|n-1}$ is the target's state error covariance matrix at time step n incorporating all the measurement up to and including time step $n-1$.

After each coherent processing interval, the received signals are centrally combined and a measurement of the target's current state is made. The measurement is filtered into the state estimate using the following equations:

$$\boldsymbol{K}_n = \boldsymbol{P}_{n|n-1}\boldsymbol{H}^T\left(\boldsymbol{H}\boldsymbol{P}_{n|n-1}\boldsymbol{H}^T + \boldsymbol{R}_n\right)^{-1} \tag{12a}$$

$$\hat{\boldsymbol{\theta}}_{n|n} = \hat{\boldsymbol{\theta}}_{n|n-1} + \boldsymbol{K}_n(\boldsymbol{z}_n - \boldsymbol{H}\hat{\boldsymbol{\theta}}_{n|n-1}) \tag{12b}$$

$$\boldsymbol{P}_{n|n} = (\boldsymbol{I} - \boldsymbol{K}_n\boldsymbol{H})\,\boldsymbol{P}_{n|n-1}\,(\boldsymbol{I} - \boldsymbol{K}_n\boldsymbol{H})^T + \boldsymbol{K}_n\boldsymbol{R}_n\boldsymbol{K}_n^T \tag{12c}$$

where $\boldsymbol{K}_n$ is the Kalman gain at time step n and the matrix $\boldsymbol{R}_n$ is the measurement covariance matrix also at time step n. The estimate of the target's state and error covariance matrix at time step n incorporating the n-th measurement is $\boldsymbol{\theta}_{n|n}$ and $\boldsymbol{P}_{n|n}$ respectively.

VI. Detection-Fusion Scheme

The Detection-Fusion scheme estimates the target's state in two steps. Firstly, each receiver individually estimates the target's bistatic time-delay and Doppler shift. The individual measurements from each receiver are then sent to a central processor where an extended Kalman filter combines the multiple time-delay and Doppler-shift measurements into a single target track.

The Detection-Fusion scheme has the advantage that only a subset of the received data is sent to the central processor, making the scheme much more practical especially for moving receivers which must rely on lower bandwidth wireless data links to the central processor.

The measurement model at time step n is given by:

$$\boldsymbol{z}_n = h(\boldsymbol{\theta}_n) + \boldsymbol{e} = \begin{pmatrix} \tau_1(\boldsymbol{\theta}_n) \\ f_1(\boldsymbol{\theta}_n) \\ \vdots \\ \tau_i(\boldsymbol{\theta}_n) \\ f_i(\boldsymbol{\theta}_n) \\ \vdots \\ \tau_N(\boldsymbol{\theta}_n) \\ f_N(\boldsymbol{\theta}_n) \end{pmatrix} + \begin{pmatrix} e_{\tau_1} \\ e_{f_1} \\ \vdots \\ e_{\tau_i} \\ e_{f_i} \\ \vdots \\ e_{\tau_N} \\ e_{f_N} \end{pmatrix} \tag{13}$$

where $\begin{pmatrix}\tau_i(\boldsymbol{\theta}_n) & f_i(\boldsymbol{\theta}_n)\end{pmatrix}^\intercal$ is the target's bistatic time-delay and Doppler-shift at the i-th receiver, and the vector $\begin{pmatrix}e_{\tau_i} & e_{f_i}\end{pmatrix}^\intercal$ is an error term modelled as a zero mean Gaussian multivariate random vector

$$\begin{pmatrix} e_{\tau_i} \\ e_{f_i} \end{pmatrix} \sim \mathcal{N}\left(\mathbf{0}, \text{CRLB}(\tau_i, f_i)\right) \tag{14}$$

where $\text{CRLB}(\tau_i, f_i)$ is the time-delay and Doppler shift CRLB which depends of the ambiguity function of the transmitted waveform and the SNR of the received signal at the i-th receiver [8].

A. Extended Kalman Filter

The Extended Kalman filter is used to combine the time-delay and Doppler-shift measurements from each receiver and determine the target's trajectory. The filters prediction step is the same as the prediction step used by the Kalman filter for the IQ-Fusion scheme (11).

After each coherent processing interval, each receiver estimates the target's relative time-delay and Doppler shift which are centrally combined (13). The measurement vector is filtered into the state estimate using the following equations:

$$\boldsymbol{K}_n = \boldsymbol{P}_{n|n-1}\tilde{\boldsymbol{H}}_n^T\left(\tilde{\boldsymbol{H}}_n\boldsymbol{P}_{n|n-1}\tilde{\boldsymbol{H}}_n^T + \boldsymbol{R}_n\right)^{-1} \tag{15a}$$

$$\hat{\boldsymbol{\theta}}_{n|n} = \hat{\boldsymbol{\theta}}_{n|n-1} + \boldsymbol{K}_n(\boldsymbol{z}_n - h(\hat{\boldsymbol{\theta}}_{n|n-1})) \tag{15b}$$

$$\boldsymbol{P}_{n|n} = \left(\boldsymbol{I} - \boldsymbol{K}_n\tilde{\boldsymbol{H}}\right)\boldsymbol{P}_{n|n-1}\left(\boldsymbol{I} - \boldsymbol{K}_n\tilde{\boldsymbol{H}}\right)^T + \boldsymbol{K}_n\boldsymbol{R}_n\boldsymbol{K}_n^T \tag{15c}$$

where h is the measurement function and $\tilde{\boldsymbol{H}}_n$ is the Jacobian matrix of the measurement function with respect to the target's state $\boldsymbol{\theta}$ defined as

$$\tilde{\boldsymbol{H}}_n = \begin{pmatrix} \frac{\partial\tau_1}{\partial x} & \frac{\partial\tau_1}{\partial y} & \frac{\partial\tau_1}{\partial z} & \frac{\partial\tau_1}{\partial \dot{x}} & \frac{\partial\tau_1}{\partial \dot{y}} & \frac{\partial\tau_1}{\partial \dot{z}} \\ \frac{\partial f_1}{\partial x} & \frac{\partial f_1}{\partial y} & \frac{\partial f_1}{\partial z} & \frac{\partial f_1}{\partial \dot{x}} & \frac{\partial f_1}{\partial \dot{y}} & \frac{\partial f_1}{\partial \dot{z}} \\ \vdots & \vdots & \vdots & \vdots & \vdots & \vdots \\ \frac{\partial\tau_N}{\partial x} & \frac{\partial\tau_N}{\partial y} & \frac{\partial\tau_N}{\partial z} & \frac{\partial\tau_N}{\partial \dot{x}} & \frac{\partial\tau_N}{\partial \dot{y}} & \frac{\partial\tau_N}{\partial \dot{z}} \\ \frac{\partial f_N}{\partial x} & \frac{\partial f_N}{\partial y} & \frac{\partial f_N}{\partial z} & \frac{\partial f_N}{\partial \dot{x}} & \frac{\partial f_N}{\partial \dot{y}} & \frac{\partial f_N}{\partial \dot{z}} \end{pmatrix}\Bigg|_{\hat{\boldsymbol{\theta}}_{n|n-1}} \tag{16}$$

which consists of the derivatives of the time-delay and Doppler-shift measurements with respect to the target's state (see the appendix for details).

VII. Case-Study

Fig. 1 shows the simulation geometry, the network consists of a monostatic radar and three bistatic receivers. The target, shown in red, moves at a constant speed following a linear path. The three receivers also move at a constant speed and follow a linear path. The target speed is defined as 20 m/s which is typical of a large fixed wing drone.

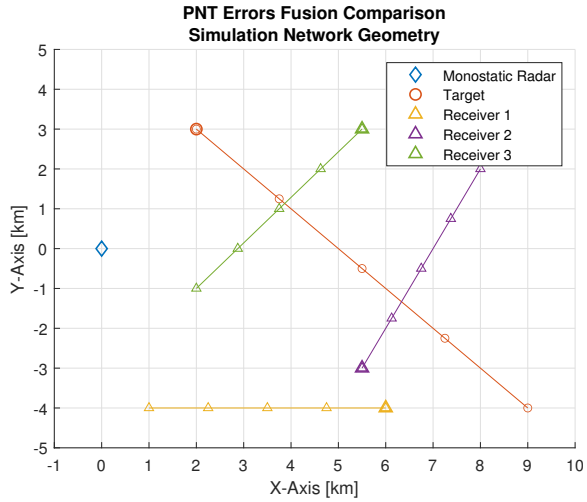

Fig. 1: Simulation Geometry

Fig. 1 also shows five sample points along the target and receiver trajectories, which are indicated by the smaller markers. At each of the these five sample points the MLE will be used to approximate the PNT-CRLB of the target's state. As the simulation progress and the target moves between the sample points the bound can be estimated by interpolating between the estimated bound at the sample points. In order simplify and reduce the amount of computation required to compute the PNT-CRLB, we assume that the received SNR for receivers is a constant 25 dB (and that therefore it is independent of the target state) and only consider a 2D simulation case, with the transmitter, target and all receivers constrained to the xy-plane. The simulation parameters are summarised in Table II.

TABLE II: Simulation Parameters

Parameter	Value
Simulation duration	500 s
Target speed	20 m/s
Receiver speed	15 m/s
Carrier frequency	1.5 GHz
Waveform	Gaussian Pulse Train
Pulse-width	1 μs
Number of pulses	16
PRF	7.5 kHz
SNR	25 dB

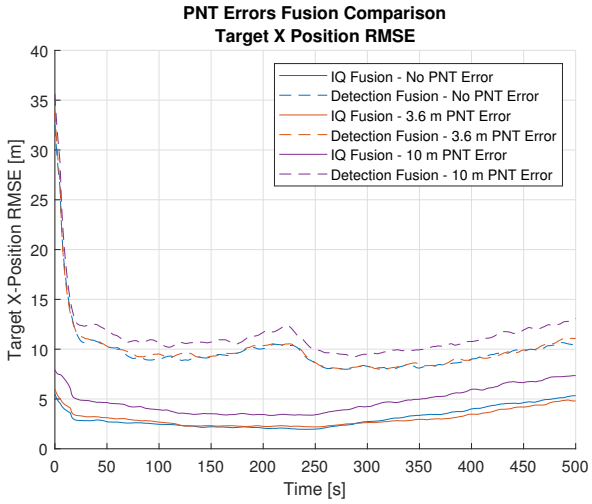

Fig. 2: Fusion Scheme Comparison with PNT Errors - Target X Position RMSE

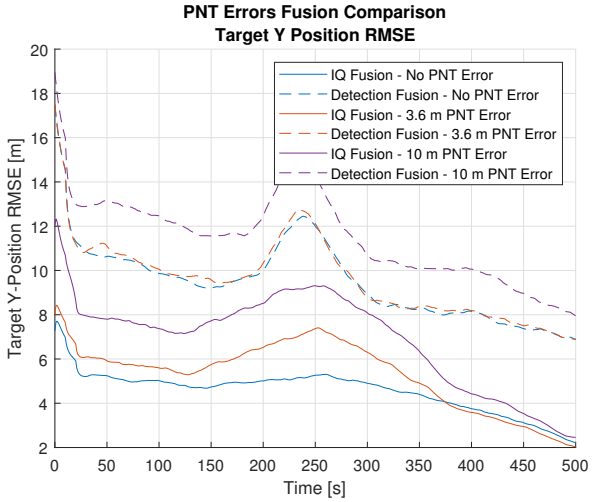

Fig. 3: Fusion Scheme Comparison with PNT Errors - Target Y Position RMSE

VIII. Simulation Results

Fig. 2 to Fig. 3 show the results of the PNT simulations. The track RMSE is averaged over 5000 Monte-Carlo trials. The track RMSE results for the IQ-Fusion scheme are shown by the solid coloured lines while the track RMSE results for the Detection-Fusion scheme are shown by the dashed lines. The different colours correspond to different levels of PNT error.

In the first few seconds of the simulations the filter initialisation behaviour is visible as a rapid decrease in the track RMSE. For example, Fig. 2 shows the x-position component of the track RMSE over time. The initial Detection-Fusion RMSE for all levels of PNT error is approximately 35 m. The Extended-Kalman filter quickly converges resulting in an approximately 10 m RMSE for the first two levels of PNT error and an average 12.5 m RMSE for a 10 m position standard deviation

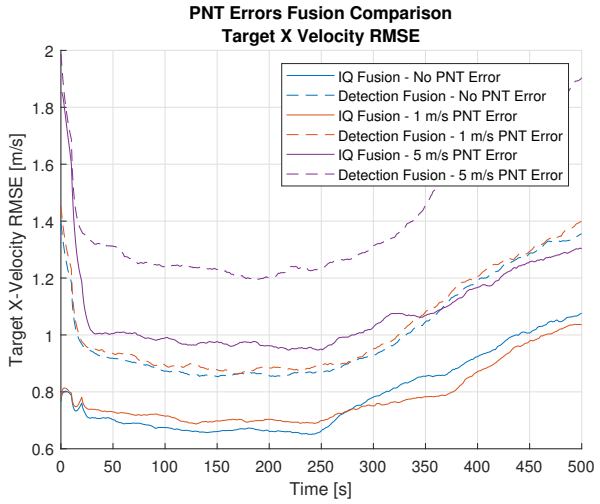

Fig. 4: Fusion Scheme Comparison with PNT Errors - Target X Velocity RMSE

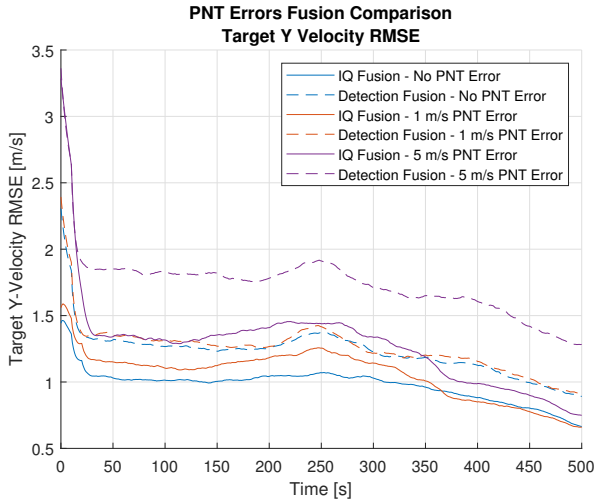

Fig. 5: Fusion Scheme Comparison with PNT Errors - Target Y Velocity RMSE

PNT error. The IQ-Fusion initialises with a significantly lower RMSE of approximately 5 m and stays relatively constant throughout the simulation. Both fusion schemes show little difference between no PNT error and a 3.6 m position standard deviation of PNT error. In both cases the increase in track RMSE over time between no PNT errors and a 10 m standard deviation PNT error is approximately 40%.

Fig. 3 shows the y-position component of the track RMSE over time. The same initialisation behaviour is present and an increase in track RMSE from both fusion schemes is visible between 200 s and 300 s. As this effects both fusion-schemes, this is most likely due to the changing geometry. In particular across both Fig. 2 and Fig. 3, the track produced by the IQ-Fusion scheme results in a track RMSE which is better than the Detection-Fusion track, even with a 10 m standard deviation PNT error.

Fig. 4 and Fig. 5 shows the velocity components of the track RMSE between the two fusion schemes. As with the position figures, the behaviour of the filter initialisation process is visible. However, in unlike the position estimates, after 250 s the track RMSE for all levels of PNT error and both fusion schemes changes, the x-velocity component of target track increases whereas the y-velocity component of the target track decreases slightly. Again this is likely due to the changing geometry. The increase in track error for the IQ-Fusion scheme is approximately 30% and 40% for the Detection-Fusion scheme between no PNT error and the maximum simulated PNT error (5 m/s standard deviation).

IX. Conclusions

In this paper the effect of PNT errors on two fusion-schemes is explored. Multiple Monte-Carlo simulations have been run across several levels of PNT error to compare two fusion schemes and quantify their resilience to PNT errors. Across all levels of PNT error, the IQ-Fusion scheme generates the track with the smallest RMSE. Remarkably, the change in track error as a function of the amount of PNT error is consistent between the two fusion schemes, and indicates that both schemes are robust. Further simulations at increasing amounts of PNT error are needed to confirm this.

A key observation is that the difference in track RMSE between the two fusion-schemes remains relatively small throughout the simulations. Note that a constant SNR of 25 dB is assumed at all receivers, and therefore it is assumed that all receivers are contributing detections. In practise this is not the case, and therefore some receivers will not detect the target. In this case the difference between the two fusion schemes is expected to be greater as the Detection-Fusion scheme performs worse due to the missed detections.

A. Future Work

The presented simulations are constrained to 2D and assume a constant SNR. This is a limitation of the modelling technique as the PNT-CRLB needs to be approximated by running Monte-Carlo trials of the MLE, which is computationally intensive. The incorporation of a variable SNR, signal multipath, and the ability to do 3D simulations requires additional investigation into methods to speed up the simulation process and/or alternative modelling approaches.

Acknowledgement

The authors express their gratitude to DSTL for funding this work under the Defence and Security Accelerator (DASA Contract Number PA0000000369 - DSTL project ACC6029850).

References

[1] M. Jahangir and C. Baker, "Persistence surveillance of difficult to detect micro-drones with l-band 3-d holographic radar™," in *2016 CIE International Conference on Radar (RADAR)*, 2016, pp. 1–5.

[2] B. Griffin, A. Balleri, C. Baker, and M. Jahangir, "Prototyping a dual-channel receiver for use in a staring cooperative radar network for the detection of drones," in *2021 21st International Radar Symposium (IRS)*, 2021, pp. 1–7.

[3] B. Griffin, A. Balleri, C. Baker, M. Jahangir, and S. Harman, "Development of a passive dual channel receiver at l-band for the detection of drones," in *2021 18th European Radar Conference (EuRAD)*, 2022, pp. 106–109.
[4] M. Jahangir, C. J. Baker, M. Antoniou, B. Griffin, A. Balleri, D. Money, and S. Harman, "Advanced cognitive networked radar surveillance," in *2021 IEEE Radar Conference (RadarConf21)*, 2021, pp. 1–6.
[5] B. Griffin, A. Balleri, C. Baker, and M. Jahangir, "Optimal receiver placement in staring cooperative radar networks for detection of drones," in *2020 IEEE Radar Conference (RadarConf20)*, 2020, pp. 1–6.
[6] M. A. Richards, *Principles of modern radar: Vol I: Basic principles*. SciTech Publishing, 2010.
[7] *Global Positioning System Standard Service Performance Standard*. United States of America Department of Defense, April 2020.
[8] H. L. Van Trees, *Detection, estimation, and modulation theory, Part I: detection, estimation, and linear modulation theory*. John Wiley & Sons, 2004.

APPENDIX

Derivatives of the bistatic time-delay with respect to the target's state:

$$\frac{\partial \tau_i}{\partial x} = \frac{1}{c}\left(\frac{x - x_0}{\sqrt{\langle \boldsymbol{U}(\boldsymbol{p}_0 - \boldsymbol{\theta}), \boldsymbol{U}(\boldsymbol{p}_0 - \boldsymbol{\theta})\rangle}} + \frac{x - x_i}{\sqrt{\langle \boldsymbol{U}(\boldsymbol{p}_i - \boldsymbol{\theta}), \boldsymbol{U}(\boldsymbol{p}_i - \boldsymbol{\theta})\rangle}}\right) \tag{17a}$$

$$\frac{\partial \tau_i}{\partial y} = \frac{1}{c}\left(\frac{y - y_0}{\sqrt{\langle \boldsymbol{U}(\boldsymbol{p}_0 - \boldsymbol{\theta}), \boldsymbol{U}(\boldsymbol{p}_0 - \boldsymbol{\theta})\rangle}} + \frac{y - y_i}{\sqrt{\langle \boldsymbol{U}(\boldsymbol{p}_i - \boldsymbol{\theta}), \boldsymbol{U}(\boldsymbol{p}_i - \boldsymbol{\theta})\rangle}}\right) \tag{17b}$$

$$\frac{\partial \tau_i}{\partial z} = \frac{1}{c}\left(\frac{z - z_0}{\sqrt{\langle \boldsymbol{U}(\boldsymbol{p}_0 - \boldsymbol{\theta}), \boldsymbol{U}(\boldsymbol{p}_0 - \boldsymbol{\theta})\rangle}} + \frac{z - z_i}{\sqrt{\langle \boldsymbol{U}(\boldsymbol{p}_i - \boldsymbol{\theta}), \boldsymbol{U}(\boldsymbol{p}_i - \boldsymbol{\theta})\rangle}}\right) \tag{17c}$$

and

$$\frac{\partial \tau_i}{\partial \dot{x}} = \frac{\partial \tau_i}{\partial \dot{y}} = \frac{\partial \tau_i}{\partial \dot{z}} = 0 \tag{18}$$

Derivatives of the bistatic Doppler-Shift with respect to the target's state:

$$\frac{\partial f_i}{\partial x} = -\frac{1}{\lambda}\left(\frac{\dot{x}}{\sqrt{\langle \boldsymbol{U}(\boldsymbol{p}_0 - \boldsymbol{\theta}), \boldsymbol{U}(\boldsymbol{p}_0 - \boldsymbol{\theta})\rangle}} + \frac{(x - x_0)\langle \boldsymbol{V}\boldsymbol{\theta}, \boldsymbol{U}(\boldsymbol{p}_0 - \boldsymbol{\theta})\rangle}{\sqrt{\langle \boldsymbol{U}(\boldsymbol{p}_0 - \boldsymbol{\theta}), \boldsymbol{U}(\boldsymbol{p}_0 - \boldsymbol{\theta})\rangle}^3} + \frac{(\dot{x} - \dot{x}_i)}{\sqrt{\langle \boldsymbol{U}(\boldsymbol{p}_i - \boldsymbol{\theta}), \boldsymbol{U}(\boldsymbol{p}_i - \boldsymbol{\theta})\rangle}} + \frac{(x - x_i)\langle \boldsymbol{V}(\boldsymbol{\theta} - \boldsymbol{p}_i), \boldsymbol{U}(\boldsymbol{p}_i - \boldsymbol{\theta})\rangle}{\sqrt{\langle \boldsymbol{U}(\boldsymbol{p}_i - \boldsymbol{\theta}), \boldsymbol{U}(\boldsymbol{p}_i - \boldsymbol{\theta})\rangle}^3}\right) \tag{19a}$$

$$\frac{\partial f_i}{\partial y} = -\frac{1}{\lambda}\left(\frac{\dot{y}}{\sqrt{\langle \boldsymbol{U}(\boldsymbol{p}_0 - \boldsymbol{\theta}), \boldsymbol{U}(\boldsymbol{p}_0 - \boldsymbol{\theta})\rangle}} + \frac{(y - y_0)\langle \boldsymbol{V}\boldsymbol{\theta}, \boldsymbol{U}(\boldsymbol{p}_0 - \boldsymbol{\theta})\rangle}{\sqrt{\langle \boldsymbol{U}(\boldsymbol{p}_0 - \boldsymbol{\theta}), \boldsymbol{U}(\boldsymbol{p}_0 - \boldsymbol{\theta})\rangle}^3} + \frac{(\dot{y} - \dot{y}_i)}{\sqrt{\langle \boldsymbol{U}(\boldsymbol{p}_i - \boldsymbol{\theta}), \boldsymbol{U}(\boldsymbol{p}_i - \boldsymbol{\theta})\rangle}} + \frac{(y - y_i)\langle \boldsymbol{V}(\boldsymbol{\theta} - \boldsymbol{p}_i), \boldsymbol{U}(\boldsymbol{p}_i - \boldsymbol{\theta})\rangle}{\sqrt{\langle \boldsymbol{U}(\boldsymbol{p}_i - \boldsymbol{\theta}), \boldsymbol{U}(\boldsymbol{p}_i - \boldsymbol{\theta})\rangle}^3}\right) \tag{19b}$$

$$\frac{\partial f_i}{\partial z} = -\frac{1}{\lambda}\left(\frac{\dot{z}}{\sqrt{\langle \boldsymbol{U}(\boldsymbol{p}_0 - \boldsymbol{\theta}), \boldsymbol{U}(\boldsymbol{p}_0 - \boldsymbol{\theta})\rangle}} + \frac{(z - z_0)\langle \boldsymbol{V}\boldsymbol{\theta}, \boldsymbol{U}(\boldsymbol{p}_0 - \boldsymbol{\theta})\rangle}{\sqrt{\langle \boldsymbol{U}(\boldsymbol{p}_0 - \boldsymbol{\theta}), \boldsymbol{U}(\boldsymbol{p}_0 - \boldsymbol{\theta})\rangle}} + \frac{(\dot{z} - \dot{z}_i)}{\sqrt{\langle \boldsymbol{U}(\boldsymbol{p}_0 - \boldsymbol{\theta}), \boldsymbol{U}(\boldsymbol{p}_0 - \boldsymbol{\theta})\rangle}} + \frac{(z - z_i)\langle \boldsymbol{V}(\boldsymbol{\theta} - \boldsymbol{p}_i), \boldsymbol{U}(\boldsymbol{p}_i - \boldsymbol{\theta})\rangle}{\sqrt{\langle \boldsymbol{U}(\boldsymbol{p}_i - \boldsymbol{\theta}), \boldsymbol{U}(\boldsymbol{p}_i - \boldsymbol{\theta})\rangle}^3}\right) \tag{19c}$$

and

$$\frac{\partial f_i}{\partial \dot{x}} = \frac{1}{\lambda}\left(\frac{x_0 - x}{\langle \boldsymbol{U}(\boldsymbol{p}_0 - \boldsymbol{\theta}), \boldsymbol{U}(\boldsymbol{p}_0 - \boldsymbol{\theta})\rangle} + \frac{x_i - x}{\langle \boldsymbol{U}(\boldsymbol{p}_i - \boldsymbol{\theta}), \boldsymbol{U}(\boldsymbol{p}_i - \boldsymbol{\theta})\rangle}\right) \tag{20a}$$

$$\frac{\partial f_i}{\partial \dot{y}} = \frac{1}{\lambda}\left(\frac{y_0 - y}{\langle \boldsymbol{U}(\boldsymbol{p}_0 - \boldsymbol{\theta}), \boldsymbol{U}(\boldsymbol{p}_0 - \boldsymbol{\theta})\rangle} + \frac{y_i - y}{\langle \boldsymbol{U}(\boldsymbol{p}_i - \boldsymbol{\theta}), \boldsymbol{U}(\boldsymbol{p}_i - \boldsymbol{\theta})\rangle}\right) \tag{20b}$$

$$\frac{\partial f_i}{\partial \dot{z}} = \frac{1}{\lambda}\left(\frac{z_0 - z}{\langle \boldsymbol{U}(\boldsymbol{p}_0 - \boldsymbol{\theta}), \boldsymbol{U}(\boldsymbol{p}_0 - \boldsymbol{\theta})\rangle} + \frac{z_i - z}{\langle \boldsymbol{U}(\boldsymbol{p}_i - \boldsymbol{\theta}), \boldsymbol{U}(\boldsymbol{p}_i - \boldsymbol{\theta})\rangle}\right) \tag{20c}$$

Multistatic dual-channel detection of drones: effects of PNT errors

Griffin, Benjamin

2023-12-28

Griffin B, Balleri A, Catherall A. (2023) Multistatic dual-channel detection of drones: effects of PNT errors. In 2023 IEEE International Radar Conference (RADAR), 6-10 November, Sydney, Australia
https://doi.org/10.1109/RADAR54928.2023.10371178